Materials Advances

ROYAL SOCIETY OF CHEMISTRY

PAPER

View Article Online
View Journal | View Issue

Cite this: *Mater. Adv.*, 2024, 5, 8588

Bio-inspired 3D printing of layered structures utilizing stabilized amorphous calcium carbonate within biodegradable matrices†

Hadar Shaked, Daniela Dobrynin, Iryna Polishchuk, Alexander Katsman and Boaz Pokroy*

Many composites in nature are formed in the course of biomineralization. These biocomposites are often produced *via* an amorphous precursor such as amorphous calcium carbonate (ACC), demonstrating a layered structure. In the current study, robocasting, a 3D-printing technique, was used to print layered structures inspired by the mineralized tissues of *Ophiomastix wendtii* and *Odontodactylus scyllarus*, which exhibit a layered organization. Various biodegradable organic matrices with a high percentage (>94%) of ACC reinforcements were compared, and their mechanical properties were studied. With the organic matrix protection, ACC was stabilized for long periods, exceeding even three years, when stored at ambient conditions. The layered structures were printed and fractured using the three-point bending method to evaluate their strength. The fracture interface was examined to weigh the benefits an amorphous precursor may offer in the 3D printing processes of ceramic materials. The fracture interface presented bulk behavior with no distinct layering, resembling the formation of mineral single crystalline tissue in nature and overcoming one of the most critical challenges in 3D printing, namely the inter-layer interfaces. Herein, a bio-inspired, low-temperature route to form layered structures is presented. By fusing the layers together following low-temperature sintering, a composite structure composed of stabilized ACC integrated with biodegradable, environmentally friendly matrices can be obtained.

Received 5th June 2024,
Accepted 24th September 2024

DOI: 10.1039/d4ma00580e

rsc.li/materials-advances

Introduction

Biomineralization is the process through which organisms form minerals in nature. Various pathways exist in different organisms to form these biominerals. These pathways include precipitation from saturated solutions, organic matrix-mediated mineralization, matrix vesicle mineralization, and amorphous-to-crystalline transformation.[1–3] The presence of an amorphous precursor is notably common in the realm of calcium carbonate ($CaCO_3$), particularly in its metastable phase, referred to as amorphous calcium carbonate (ACC).[4–6] It facilitates the formation of mechanically strengthened and intricately shaped crystals in marine organisms.[7,8] Often, ACC also serves as a precursor to crystalline $CaCO_3$, thereby permitting the incorporation of impurities at concentrations well beyond their thermodynamic solubility limit. A commonly observed impurity in $CaCO_3$ biominerals is Mg, which can be incorporated at concentrations as high as 40 at%,[9–11] considerably surpassing its thermodynamic solubility of approximately 2 at%.[12] An exemplary demonstration is found in the brittle star *Ophiomastix wendtii* (*O.wendtii*). The *O.wendtii* calcitic microlenses are formed through the transformation from ACC to a crystalline structure.[13] Previous studies on *O. wendtii*'s micro- and nanostructure discovered that the optical lenses' calcite single crystals present a complex structure integrating Mg-poor matrix (~13 mol%) and coherent Mg-rich nanometric inclusions (~40 mol%).[14,15] These inclusions are not randomly dispersed within the crystalline lenses but rather form an arched-shaped layered arrangement demonstrating periodic distances between Mg-rich and Mg-poor layers. Such a layered pattern is not unique to the *O. wendtii*, but can be seen rather frequently in nature.[16] Another example in which layered structures are employed to enhance the mechanical performance is the *Odontodactylus scyllarus* (*O. scyllarus*) dactyl club. A layered structure with two mechanically distinct regions was observed in the latter.[17,18]

The biocomposite layered structures, such as those observed in *O. wendtii* and *O. scyllarus*, along with the use of amorphous precursors, inspired the development of the current paper, which focuses on studying synthetic organic-ACC 3D printed

Department of Materials Science and Engineering and the Russell Berrie Nanotechnology Institute, Technion – Israel Institute of Technology, 32000, Haifa, Israel. E-mail: bpokroy@technion.ac.il

† Electronic supplementary information (ESI) available. See DOI: https://doi.org/10.1039/d4ma00580e

composites. Formation of 3D-layered structures has become increasingly common owing to the prevalent adoption of 3D printing, allowing the sequential deposition of layers and offering convenience and time efficiency in additive manufacturing. Owing to the growing demand for ceramic materials, numerous 3D-printing methods tailored specifically for ceramics, and ceramic composites have emerged.[19–23] Robocasting, a slurry-based additive manufacturing method where a viscous ceramic or composite slurry is extruded through a nozzle to create 3D structures layer by layer, has proved to be one of the most straightforward and widely employed techniques for 3D printing for ceramic materials. In robocasting, an externally mixed paste with various viscosities and solid loadings is used for printing. The process allows precise control over the object's geometry. However, robocasting is constrained to pastes exhibiting specific properties, such as shear-thinning behavior for extrusion, self-support post-printing, controlled agglomeration requiring pre-dispersion, and binders and dispersants that can be easily removed if a dry 3D-printed model is desired. Robocasting yields a ceramic green body that typically undergoes a sintering stage designed to remove binders and dispersants, eradicate pores, and fuse the ceramic particles. An efficient sintering process generally requires heating to temperatures ~50%–75% of the ceramic melting points. For example, alumina, a commonly used ceramic material, has a melting point of 2072 °C while sintering temperatures typically range between 1200–1700 °C.[24–26] The use of $CaCO_3$ in 3D printing is limited, often serving as an additive to bio-cements[27,28] and scaffolds[29] due to its low decomposition temperature, limiting its suitability for classical sintering processes. A primary challenge in 3D printing overall, and especially in the 3D printing of ceramic materials, lies in managing the interfaces between the printed layers. The interfacial area introduces anisotropy to the printed model and compromises its strength in the direction perpendicular to the stacked layers.[30] Numerous suggestions have been proposed to address surface defects in the layers, including the use of a glue paste,[31] the incorporation of additives in the slurry such as silica fume,[32] fly ash[33] and nano-SiO_2,[34] and the incorporation of polymers.[35] However, all the proposed solutions necessitate alterations to the layers and structure of the printed model. In this context, we propose the utilization of Mg-stabilized ACC powder. It has been demonstrated that Mg plays a cardinal role in stabilizing ACC over extended durations, preventing its crystallization, and can serve as an ink for 3D printing processes.[36] ACC allows aggregation and consolidation of particles through low-temperature diffusion facilitated by substantial amounts of structural water in the ACC. This approach results in the curability of the rough interfaces between the layers during the sintering phase.

Materials and methods

ACC powder preparation

Aqueous solutions of $CaCl_2{\cdot}2H_2O$ (147 g in 1 L), $MgCl_2{\cdot}6H_2O$ (203.31 g in 1 L), and Na_2CO_3 (52.995 g in 0.5 L) at a concentration of 1 M were prepared and cooled overnight at 8 °C. Ratios of 40/60, 50/50, and 60/40 of Ca/Mg solutions were mixed in a glass beaker for 5 minutes. An equivalent amount of Na_2CO_3 solution was added to the beaker with active mixing, maintaining a 1 : 1 ion ratio between CO_3^{-2} and $(Ca^{2+} + Mg^{2+})$. The resulting suspension was swiftly filtered through a Buchner funnel using a grade 5 Whatman filter paper, followed by washing with 600 mL of water and 200 mL of acetone. After maintaining suction for 10 minutes, the filtered powder was dried for 3 hours in a vacuum oven at 25 °C and 0.1 MPa. The dried ACC powder was then immersed in an excess of acetone and stored for up to one week.

Paste preparation with various binders

The stored Mg-ACC powder was dried, ground with a mortar and pestle, followed by mixing with a dispersant (comprising commercial corn oil at a fixed ratio of 0.1 mL per 1 g of powder) and a mixture of various organic polymers and ethylene glycol (99.8%, AR, Merck). Four different organic polymers were added in 15% w/w to ethylene glycol: commercially available pure bovine collagen, methylcellulose 15 cPs (Alfa Aesar), methylcellulose 400 cPs (Alfa Aesar), and polymerizable D-(+)-glucose (99.5%, Sigma-Aldrich). Collagen was added in weight percentages ranging from 5 to 20% w/w. The powder was gradually added to the binder and hand-mixed until a solid, firm paste was obtained. The solids-loading of the mixed paste was always maintained at 62.5%, meaning 1 g of powder for every 0.6 mL of dispersant–binder mixture. Subsequently, the pastes were loaded into the printing tubes and centrifuged at a rate of 4000 rpm for 20 minutes to degas.

3D printing and post-processing

3D models were formed using a commercially available Hyrel 3D – Engine-SR printer with two KR2-15 stainless steel extrusion heads comprising 1 mm nozzles. 3D-computer-aided design (3D-CAD) of the printed models was sketched using Fusion 360 (Autodesk) following ASTM C1161 – 18 configuration C.[37] The 3D-CAD was converted into an STL file, which was uploaded to the printer, where it was sliced, and the G-code was written. The G-code was then modified to enable printing with two printing heads and alternating layers. The printed models were placed in a vacuum oven for low-temperature sintering overnight at 150 °C and a vacuum level of 0.1 MPa.

Beam strength measurements

The printed models were prepared following the specifications of configuration C in ASTM C1161 – 18. In this configuration, the specimen dimensions are as follows: length 90 mm, width 8 mm, and depth 6 mm. Subsequently, the specimen was positioned in a three-point flexure fixture, where the two support beams are free to roll, and the middle bearing remains stationary. Still, it can be articulated to align with the model's top surface. The support beam was secured at a specified distance of 80 mm, as outlined in the ASTM standard. Five printed specimens were tested, fitting the breakage pattern eligible for calculations, as breakage formed where the pressure

was enforced in the middle of the beam. Calculations were performed using the following equation of the strength in three-point flexure:

$$S = \frac{3}{2} \cdot \frac{PL}{2bd^2} \quad (1)$$

where P is the measured break force (in N), L is the outer support span, b is the specimen width, and d is the specimen thickness (in m).

The standard deviation between the measurements was calculated as follows:

$$\mathrm{SD} = \sqrt{\left(\frac{\sum_{1}^{n}(S-\bar{S})^2}{n-1}\right)} \quad (2)$$

where $\bar{S}$, the mean value of the calculated beam strength, is calculated as follows:

$$\bar{S} = \frac{\sum_{1}^{n} S}{n} \quad (3)$$

where n is the number of examined specimens.

The printed specimens were inspected using an Instron 3345 Series Single Column Table testing system, with a 50–5000 N loading cell, calibrated with an error range of 0.02 N and with a loading rate of 0.3 mm min^{-1}.

The Young's modulus and the strain energy were calculated using OriginPro 2019 (OriginLab Corporation, Northampton, MA, USA).

High-resolution scanning electron microscopy

The samples were imaged using the Zeiss Ultra-Plus FEG-SEM at 1–2 keV with a working distance of 4–4.2 mm. Energy-dispersive X-ray spectroscopy (EDS) was conducted at 9 keV with an 8.4 mm working distance.

High-resolution synchrotron powder X-ray diffraction (HRPXRD)

HRPXRD experiments were conducted on the ID22 beamline at the European Synchrotron Research Facility (ESRF) in Grenoble, France. The experiments were carried out at a wavelength of 0.3542 Å. Samples were loaded into borosilicate capillaries, and their high-resolution XRD patterns were collected.

Lab X-ray diffraction

The diffraction pattern for the 40/60CGN15% model powdered sample was obtained using the Rigaku SmartLab 9 kW high-resolution diffraction system, at a wavelength of Cu K-α 1.5406 Å.

Thermogravimetric analysis

Thermogravimetric analysis was conducted using the TGA/DSC 3+ instrument from Mettler Toledo. A ceramic crucible was employed, and a small quantity of powder was added. The powder was subsequently heated to 700 °C under a nitrogen environment.

The calculation of evaporated water during the oven drying stage was carried out as follows:

$$\text{Evaporated water}_{\text{oven drying}} = \left(1 - \frac{\text{Water in ACC sample}}{\text{Water in printed sample(ACC + collagen)}}\right) \times 100\% \quad (4)$$

Micro-computed tomography (Micro CT)

Micro-computed tomography was performed using the NeoScan N80. A sample of the 3D printed model was affixed to the rotating stage, aligned, and scanned using a 67 kV voltage, 59 μA power, and a 0.5 aluminum filter.

Dynamic light scattering (DLS)

The hydrodynamic diameter (D_h) and the polydispersity index (PDI), (nanoparticle size distribution) were measured by DLS at a scattering angle of 173°, utilizing Zetasizer Nano-ZS, Malvern Instruments, Malvern, UK. 0.5 g of ACC powders with 40/60, 50/50, and 60/40 Ca/Mg ratios were dispersed in 23 mL of acetone for 30 minutes in a bath sonicator. The suspension was then filtered using SRP15 Syringe Filter 17559 to avoid the passage of agglomerates. The suspension was rapidly measured after mixing in a quartz cuvette.

Results and discussion

ACC pastes used in this research were prepared based on a protocol previously described by our group.[36] Ethylene glycol (EG) was chosen as the base binder owing to its non-toxic behavior and ability to preserve the amorphous nature of the ACC powder over time. Various natural additives were incorporated into EG in a 15% w/w ratio, formulating printable ACC pastes comprising ACC powder with a Ca/Mg ratio of 50/50. The additives included collagen (50/50CGN15%), glucose (50/50Glu15%), methylcellulose 15 cPs (50/50MCL_15), and methylcellulose 400 cPs (50/50MCL_400). The addition of collagen was subsequently studied by mixing ACC Ca/Mg 50/50 powder with 5% w/w collagen in EG (50/50CGN5%), 10% w/w collagen in EG (50/50CGN10%), and 20% w/w collagen in EG (50/50CGN20%). Two additional pastes were formed, one using ACC Ca/Mg 60/40 powder with 15% w/w of collagen in EG (60/40CGN15%) and another with ACC Ca/Mg 40/60 powder with 15% w/w of collagen in EG (40/60CGN15%). Sample abbreviations are summarized in Table 1. Organics-ACC pastes were formed by combining the additive-rich EG solution with ACC powder, resulting in a high solid loading of approximately 65 w/w% ACC. The pastes were then used to print beams measuring 90 mm in length, 8 mm in width, and 6 mm in height. Subsequently, they were dried in a vacuum oven overnight and sintered (150 °C, 0.1 MPa, 15 h). The resulting dry composite models comprised an ACC reinforcement and an organic matrix. Models with a 20% w/w collagen ratio consisted of a composite composed of 93% reinforcement and 7% matrix,

Table 1 Summary of sample abbreviations comprising materials, powder, additive, and additive percentage

Sample	Ca/Mg ACC Powder	Additive	Additive in EG [w/w%]
50/50CGN15%	Ca/Mg 50/50	Collagen	15
50/50Glu15%	Ca/Mg 50/50	Glucose	15
50/50MCL_15	Ca/Mg 50/50	Methylcellulose 15 cPs	15
50/50MCL_400	Ca/Mg 50/50	Methylcellulose 400 cPs	15
50/50CGN5%	Ca/Mg 50/50	Collagen	5
50/50CGN10%	Ca/Mg 50/50	Collagen	10
50/50CGN20%	Ca/Mg 50/50	Collagen	20
60/40CGN15%	Ca/Mg 60/40	Collagen	15
40/60CGN15%	Ca/Mg 40/60	Collagen	15

models with a 15% w/w collagen ratio consisted of a composite composed of 94.75% reinforcement and 5.25% matrix, models with a 10% w/w collagen ratio consisted of a composite composed of 96.5% reinforcement and 3.5% matrix, and models with a 5% w/w collagen ratio consisted of a composite composed of 98.25% reinforcement and 1.75% matrix.

The morphology and crystallization state of the models was then tested, as depicted in Fig. 1. The spherical morphology of the ACC was retained after the sintering step (Fig. 1(A)–(H)) in all 3D-printed models. HPXRD diffractograms confirmed that all models remained amorphous after the oven-drying process (Fig. 1(I)). The diffraction peaks in Fig. 1(I) stem from NaCl byproducts; a calcite diffractogram is presented for reference. Adding organic matrices to all presented ACC powders (with Ca/Mg ratios of 50/50, 60/40, and 40/60) allowed increased stabilization of the ACC's amorphous nature for a period exceeding three years when stored at ambient conditions (Fig. S2, ESI†).

To assess the beam strength (BST) under ambient conditions, the printed models were subjected to a three-point bending (3PB) test following ASTM 1161-18, configuration C.[37] The beam dimensions were as follows: length 90 mm, width 8 mm, and depth 6 mm, with an inner span of 80 mm—initially, 50/50 ACC powder models with a 15% w/w additive-rich EG solution were tested and compared. Calculations were conducted according to eqn (1)–(3) as described in the Materials and Methods section. As depicted in Fig. 2, 50/50CGN15% exhibited the highest BST among 50/50MCL_15, 50/50MCL_400, and 50/50GLU15%. Further steps were taken based on the outstanding results obtained from the 50/50CGN15% model.

First, various CGN concentrations were tested, ranging from 5 to 20% w/w. Increased BST was observed in the case of models with higher CGN concentration, reaching a peak in the 50/50CGN15% model followed by a plateau in the 50/50CGN20% model, thus, the 50/50CGN20% was omitted (Fig. S1, ESI†).

Additionally, given CGN 15%w/w additive exhibits the most superior mechanical properties, it was combined with Ca/Mg 60/40 powder (60/40CGN15%) and Ca/Mg 40/60 powder (40/60CGN15%). The mechanical strength of the 60/40CGN15% printed model was further enhanced; conversely, fusion with Ca/Mg 40/60 powder led to diminished mechanical strength

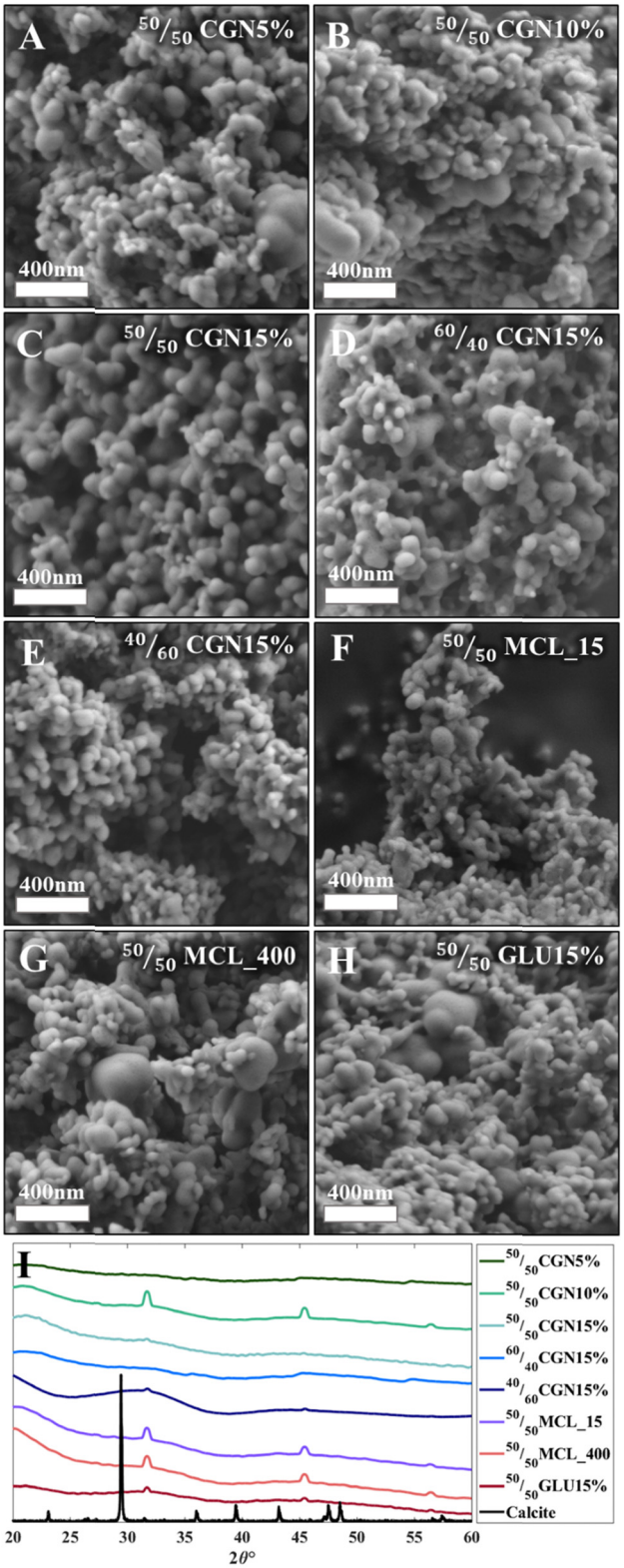

Fig. 1 (A)–(H) HR-SEM images depict ACC 3D-printed models with various additives after sintering. ACC powders with additive-rich environments are shown as follows: (A) 50/50CGN5%; (B) 50/50CGN10%; (C) 50/50CGN15%; (D) 60/40CGN15%; (E) 40/60CGN15%; (F) 50/50MCL_15; (G) 50/50MCL_400 and (H) 50/50Glu15%. (I) HRPXRD patterns were collected at a wavelength of Cu Kα 1.546 Å and a wavelength of 0.3542 Å, normalized to Cu Kα.

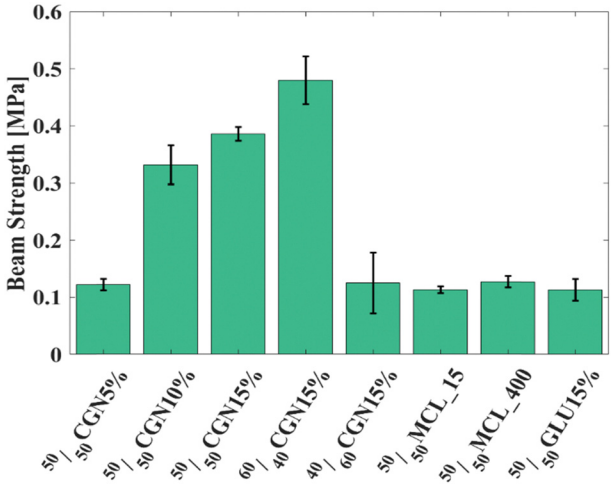

Fig. 2 BST of organics-ACC models with single-material matrix. 60/40CGN15% presents the highest BST.

compared to that of 50/50CGN15%. Among the tested models, and in the CGN series specifically, 60/40CGN15% presented relatively superior mechanical properties. This result is opposite to what occurs in nature, where a higher concentration of Mg-rich inclusions in a crystalline $CaCO_3$ structure results in a higher strength compared to that of lower-Mg content crystalline $CaCO_3$.[14] Stress–strain curves of all tested models are depicted in Fig. S3A–I (ESI†). Additive-free EG models have also been tested yet were deemed unsuitable, as they yielded unmeasurable results. These models fractured upon the slightest contact between the pressing bearing and the model, indicating a flexural strength below the measurable 0.006 MPa.

For a comprehensive understanding of the Ca/Mg ratio dependency in the ACC powder (Ca/Mg ratios of 40/60, 50/50 and 60/40), the presence of entrapped structural water in the amorphous structure was analyzed using thermogravimetric analysis (TGA). Table 2 illustrates TGA results revealing the difference in behavior between Ca/Mg 50/50, 60/40 and 40/60 ACC powders and their corresponding collagen 15%w/w models 50/50CGN15%, 60/40CGN15%, and 40/60CGN15% occurring between 25 and 600 °C. The TGA results obtained from the ACC powders can be correlated with the amount of structural water entrapped within each powder: 18.77% in the case of 40/60ACC powder, 37.39% in the case of 50/50 ACC powder, and 48.87% in the case of 40/60 ACC powder. During the initial heating stage (50–150 °C), the ACC powder retains its amorphous state while structural water evaporates, leaving behind dry ACC. Around 400 °C, crystallization occurs, accompanied by minimal removal of structural water, aligning with findings from previous studies.[38] The amount of incorporated Mg in the ACC directly correlates with the content of structural water; the lower the level of incorporated Mg in the ACC, the higher the structural water content. Following the oven drying process, the structural water content measured was 9.94% for 40/60CGN15%, 23.33% for 50/50CGN15%, and 20.14% for 60/40CGN15%. The percentage of evaporated water during the oven drying stage was calculated as outlined in eqn (4). During the oven drying process, 47.04%, 37.6%, and 58.79% of the structural water, entrapped within the ACC structure, evaporated from the 40/60CGN15%, 50/50CGN15% and, in the 60/40CGN15% models, accordingly. The highest strength observed in the 60/40CGN15% (Fig. 2) can be attributed to the fact that a significant amount of water, initially present in the 60/40 ACC powder, evaporated during the oven drying process (Table 2). The effect of the enhanced strength is, therefore, probably a result of water-enhanced diffusion in the 60/40CGN15%.

The higher amount of structural water released during the 60/40CGN15% drying process may also contribute to enhanced aggregation and consolidation of the ACC particles, resulting in a more uniform 3D-printed model. The latter effect could also influence the final BST. The influence of Mg concentration on the amount of structural water is still unknown, yet the impact of both Mg and water on the crystallization has been previously studied.[39] While Mg stabilizes the amorphous state of ACC, water accelerates the crystallization process. It has been assumed that the structural water bound to Mg ions increases Mg-ACC stability.[40] This assumption, however, contradicts our results.

To follow the variations in aggregation and consolidation between the ACC powders, DLS measurements were performed for the 40/60, 50/50, and 60/40 ACC powders as well as for their corresponding collagen 15w/w% models: 40/60CGN15%, 50/50CGN15% and 60/40CGN15% (Table 3). As can be deduced from the results, the size of powdered ACC particles ranges between 4–7 nm for all samples prior to the low-temperature sintering step, and an increase in particle size can be observed as the Mg amount decreases. This observation suggests that the aggregation and consolidation process is more prevalent at a lower Mg content, characteristic for the models showing increased amount of evaporated structural water. The obtained

Table 2 The quantities of evaporated water during the low-temperature sintering stage, calculated from TGA analysis, for Ca/Mg 50/50, 60/40 and 40/60 ACC powders, and the corresponding CGN15% composites

Sample	Structural water [%]	Water in the tested sample [%]	Evaporated water during oven drying process [%]
40/60 ACC powder	10.99 (initial) 7.88 (crystallization)	18.77	47.04
40/60CGN15% model	7.22 (initial) + 2.72 (crystallization)	9.94	
50/50ACC powder	28.26 (initial) + 9.13 (crystallization)	37.39	37.6
50/50CGN15% model	15.92 (initial) + 7.41 (crystallization)	23.33	
60/40ACC Powder	45.32 (initial) + 3.55 (crystallization)	48.87	58.79
60/40CGN15% model	11.83 (initial) + 8.31 (crystallization)	20.14	

Table 3 DLS measurements of ACC and 3D printed models, illustrating changes in particle size before and after the oven drying stage

Sample	Particle size (nm)	PDI	Fold change
40/60ACC powder	6.85 ± 0.59	0.64	7.46
40/60CGN15% model	51.15 ± 5.55	0.47	
50/50 ACC powder	4.62 ± 0.91	0.34	51.49
50/50CGN15% model	237.90 ± 58.08	1	
60/40ACC Powder	4.27 ± 1.34	0.24	64.19
60/40CGN15% model	274.10 ± 74.26	0.86	

PDI is higher than expected for a monodispersed distribution in all samples, which can be explained by the ACC instability and the tendency of the particles to agglomerate.[41]

Two bio-inspired case studies have been considered based on the obtained results. The first case study, inspired by the Mg distribution in the *O. wendtii* brittle star, involves layering of ACC pastes with varying Mg content akin to the naturally occurring distribution.[14,15] Mg content variations were achieved using two different pastes, 50/50CGN15% and 60/40CGN15%. Corresponding layering patterns (LP) can be seen in Fig. 3(A)–(C) namely, LP1, LP2 and LP3. The second case study, inspired by the *O. scyllarus* dactyl club, involves the formation of layered blocks, exhibiting low and high Young's modulus.[17] This is achieved using 50/50CGN5% and 50/50CGN15% pastes. LP is depicted in Fig. 3(D)–(F) namely LP4, with 5 × 4 layering, LP5 with 6 × 3 layering and LP6 with 7 × 2 layering, of 50/50CGN5% and 50/50CGN15%, accordingly. An example of a 3D-printed beam can be seen in Fig. 3(G).

Mechanical measurements of the first case-study layered structures (Fig. 4(A)–(C)) revealed that by layering 50/50CGN15% and 60/40CGN15% according to LP1, LP2, and LP3, the Young's modulus of the resulted structure increases compared to that of the original 50/50CGN15% model and peaks at LP2 (Fig. 3(B)). LP2, where the gap between the first two 60/40CGN15% layers, compared with the gap between the first and the farthest 60/40CGN15% layers is ~0.25, most closely resembles the strengthening mechanism in the *O. wendtii*.[15] BST measurement results of the LP2 structure are of the same value as those of the 60/40CGN15% models. The difference in the strain energy is within the error range. LP2's mechanical properties slightly improved compared to those of 60/40CGN15%, indicating the importance of integrating the mechanically distinct layers and their arrangement. Mechanical measurements of the layered structures from the second case-study (Fig. 4(D)–(F)) revealed that by increasing the ratio between 50/50CGN5% and 50/50CGN15% layers, according to LP4, LP5 and LP6 (5 × 4, 6 × 3 and 7 × 2 ratio respectively) an increase in Young's modulus can be achieved, with a maximum value observed in the cases of LP5 and LP6. BST value increases with the number of 50/50CGN15% layers, where 50/50CGN15% and LP4 have approximately the same BST. The strain energy values also increase with the number of 50/50CGN15% layers, where the strain energy value of the LP4 layered structure exceeds that of 50/50CGN15%. The aforementioned results indicate that LP4 and LP5 layered structures have similar or enhanced results compared to the 50/50CGN15% model. The *O. scyllarus* dactyl club presents a ratio of 0.38 between the region with the highest Young's modulus and the entire dactyl club.[17] Due to printing limitations, achieving the same ratio between the 50/50CGN15% layers and the overall layers cannot be reached; it ranges between 0.33 and 0.44 (LP4 and LP5 structures, respectively). The LP4 and LP5 layered structures do not fall short of the 50/50CGN15%, with less organic matrix in the final product. The received results on effective Young's modulus in both case studies deviate from the expected results according to

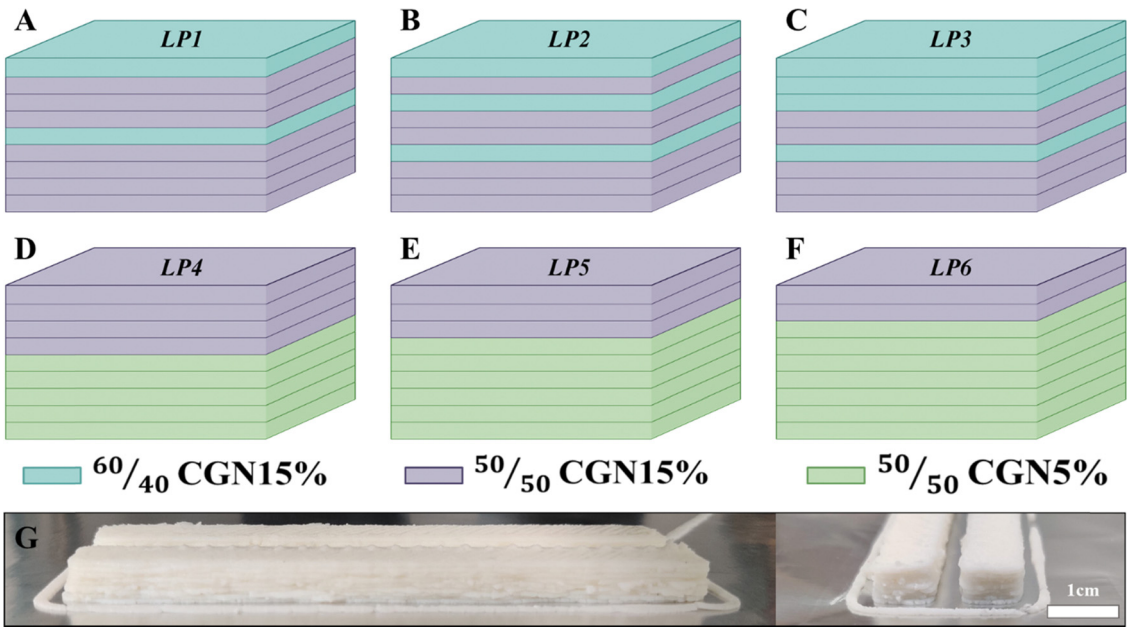

Fig. 3 (A)–(C) 50/50CGN15% and 60/40CGN15% tested layered structures, inspired by the *O. wendtii* brittlestar. (D)–(F) 50/50CGN15% and 50/50CGN5% layered structure inspired by the O. scyllarus dactyl club (G) a printed sample.

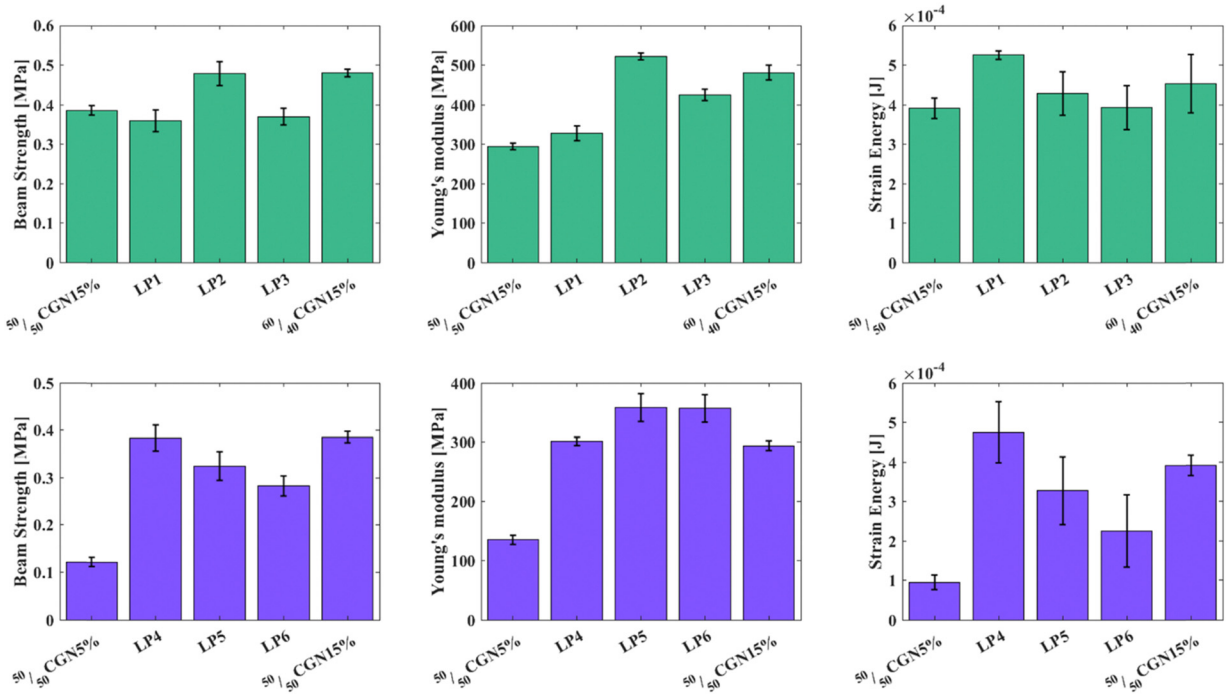

Fig. 4 Mechanical properties of *O. wendtii* (A)–(C) and *O. scyllarus* (D)–(F) inspired models. (A) BST measurements (B) Young modulus and (C) strain energy graphs of 50/50CGN15% and 60/40CGN15% models dispersed in various layered structures. (D) BST measurements (E) Young modulus and (F) strain energy graphs of 50/50CGN15% and 50/50CGN15% models dispersed in various layered structures.

the rule of mixtures. While LP1 closely follows the rule of mixtures the deviation in LP2 is higher by 54%, in LP3 by 19%, and is much more significant in LP4–LP6 where the deviations are higher by 70%, 117%, and 132% accordingly. These deviations are apparently due to the features of layered structures when stress concentrations are developed in the formed contact layers. In such cases, the effective Young's modulus can significantly exceed the values calculated according to the mixture formula as was demonstrated by Turusov *et al.*[42] in their simplified model. Enlarged value of beam strength of the LP2 model is probably also connected with the peculiarities of contact layers where additional concentration and relaxation of stresses may occur. Stress–strain curves of the layered structures are depicted in Fig. S3J–O (ESI†), an example of Young's modulus and strain energy calculations can be seen in Fig. S4 (ESI†).

While no exceptional improvement can be seen in the mechanical properties presented above, layering lower-strength materials with less Mg content/lower additive amount in a specific manner with materials that possess more Mg content/higher additive amount, no deterioration in mechanical properties is received. This shows that the internal ordering of the final product deeply influences the mechanical properties.

Reviewing the breakage surface of the 3D printed models revealed that while one of the most common defects and failure points of 3D printed models is the interface between the layers, layering was not visible at the breaking point of the aforementioned models.[30] Commonly, a high-temperature sintering process is applied in ceramics to overcome the interface defects and encourage particle coarsening. $CaCO_3$ cannot go through the traditional sintering process as calcite its most stable phase decomposes to CaO and CO_2 at 825 °C, a temperature lower than required to enable sintering.[38,43] Another limitation is the presence of organics, which burns at ~300 °C, limiting the temperature even further. During the low-temperature sintering step in our case, two processes occur: first, EG and oil evaporate while the ACC particles move towards each other due to degradation of the organic matrix, resulting in a dry composite composed mainly of inorganic ACC aggregates and a small number of organics; second, ACC-particles consolidate due to short-range diffusion in the near-interface regions resulting in a continues bulk material. Such diffusion is probably enabled due to a relatively large amount of structural water in the ACC particles. ACC allows the release of structural water, thus enabling low-temperature sintering. In Fig. 5(A), a breakage surface of the LP2 sample, resulting from a 3PB measurement, can be seen. Layering defects are not visible except for one highlighted in a purple square; the surface of a lower layer was not covered due to an air bubble in the printing piston deposited in the layer above it. The Ca/Mg distribution in LP2 was measured using EDS and can be seen in Fig. 5(B); these changes in distribution reflect the diffusion occurring during the drying process, resulting in a fluctuating curve. In Fig. 5(C), a breakage surface of the LP3 sample can be seen. While visible, defects are disrupted and not considered as layering defects. The Ca/Mg distribution in LP3 can be seen in Fig. 5(D). Higher Mg concentration is seen in the 50/50CGN15% layers compared to the 60/40CGN15% layers; a distinct step around the location where the different layers interact is visible, implying that the

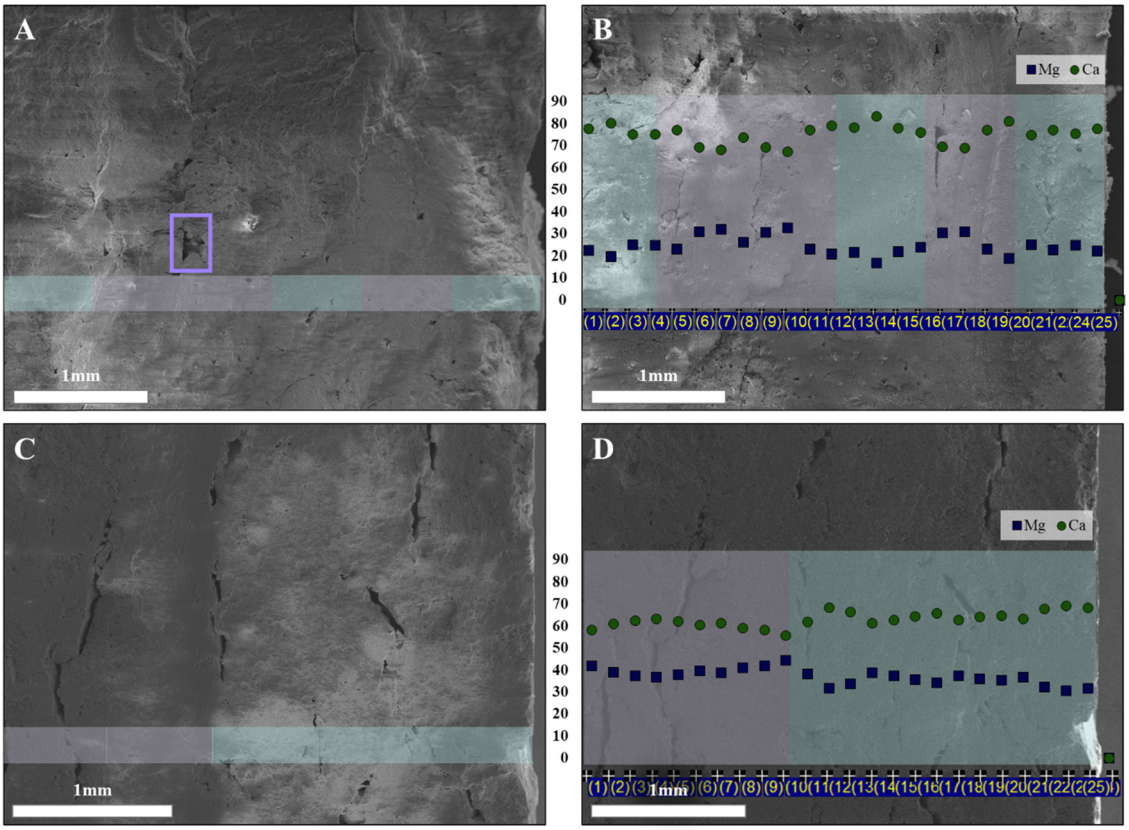

Fig. 5 (A) breakage surface of LP2 sample, resulting from a 3PB measurement. (B) EDS measurement LP2. (C) breakage surface of LP3 sample, resulting from a 3PB measurement. (D) EDS measurement LP3. Green circles – Ca ions, Purple squares – Mg ions. Colored line represents the layered structure according to LP2and LP3, light blue –layers 60/40CGN15% and purple –50/50CGN15%.

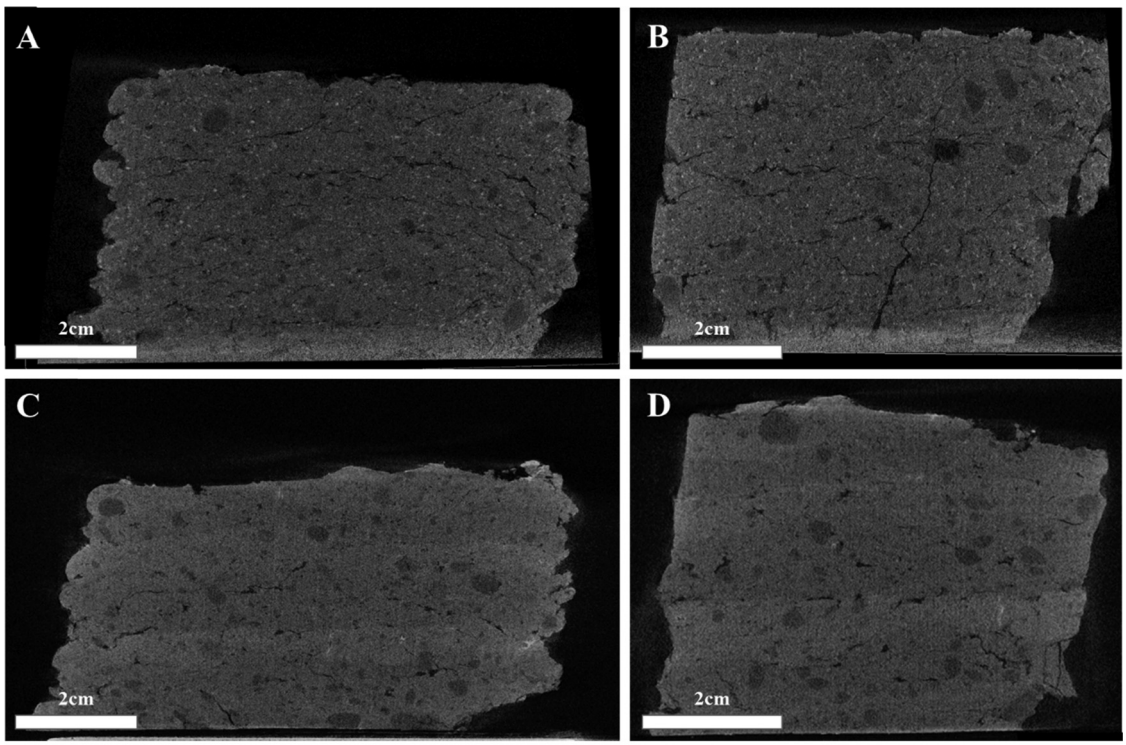

Fig. 6 MicroCT imaging of 60/40CGN15% model (A) front and (B) side view and LP2 model (C) front and (D) side view.

changes at this region and at the interfaces between the different layers in LP2 relate to the aggregation and consolidation processes.

Layers' uniformity was further investigated using Neoscan80 micro CT, a piece of 60/40CGN15%, and a piece of LP2 3D printed models have been imaged and are depicted in Fig. 6(A)–(D). In the case of 60/40CGN15% (Fig. 6(A) and (B)), a bulk-like formation can be seen, while both pores and cracks are observed, none trace the deposited layers. In the case of LP2 (Fig. 5(C) and (D)), a change in the layers' density is observed, corresponding to varying Mg content of each layer, lighter, with lower Mg content, corresponding to 60/40CGN15% layers, and darker corresponding to 50/50CGN15% layers. Though the layer alteration is visible, the interface displays as a continuous bulk, and no interlayer defect can be seen. Cracks and pores can be seen throughout the different layers with no centering around the layer's interfaces. Both cases further strengthen the claim of interlayer aggregation and consolidation process around the layers' interfaces. In Fig. 6, pores can be seen throughout the model. Pores can play an important role in ceramics, altering the mechanical properties and weakening the formed models. Volumetric pore analysis revealed porosity of 7.6% in 60/40CGN15% model, 3.9% in 50/50CGN15% model, and 6.7% in LP2 model. Pore analysis for a single slice, and size distribution of pores are given in Fig. S5 (ESI†). As can be seen, the porosity does not correlate with the strength of the models (the most porous model 60/40CGN15% has the highest strength). This allows us to conclude that the presence of pores, while significant, is not the main strengthening mechanism in the formed models and can be neglected, compared to the particles' interactions.

Conclusions

This study presents a bio-inspired approach to 3D-print biodegradable ACC composites, resembling naturally occurring layered structures. The stabilized ACC powder underwent further extended stabilization under ambient conditions, surpassing three years, by introducing organic environments resembling those found in nature. The resulting composites comprised high amounts of ACC reinforcement ($>94\%$) and a small amount of the organic matrix. The results of this work highlight the importance of even scarce organic matrix in prolonged stabilization of the printed models and their mechanical properties. Printing of layered structures composed of different ACC reinforcements, inspired by those of the *O. wendtii* optical lenses and the *O. scyllarus* dactyl club, revealed that while layering lower-strength materials in a specific manner with materials that possess higher strength, no deterioration in mechanical properties is received. Using an amorphous phase overcame a long-standing problem common in 3D printing, namely failure at the inter-layer interfaces. ACC and its capability to undergo aggregation and consolidation at relatively low temperatures due to structural water-induced diffusion resulted in a continuous bulk of the printed model, resembling the formation of single crystalline organs in nature. This bio-inspired layered 3D-printing approach ratified the significance of layering in mechanical performance of a structure. The use of ACC proved to overcome one of the most burning issues in 3D-printing and may offer a new approach for 3D-printing of powdered and ceramic materials.

Data availability

Data are available upon request from the authors.

Conflicts of interest

There are no conflicts to declare.

Acknowledgements

We thank Prof. Alejandro Sosnik for the provision of DLS facilities. The Authors acknowledge the European Synchrotron Radiation facility for the provision of synchrotron radiation facilities at ID22.

References

1 S. Weiner and L. Addadi, Crystallization pathways in biomineralization, *Annu. Rev. Mater. Res.*, 2011, **41**, 21–40, DOI: **10.1146/annurev-matsci-062910-095803**.
2 S. Weiner, J. Mahamid, Y. Politi, Y. Ma and L. Addadi, Overview of the amorphous precursor phase strategy in biomineralization, *Front. Mater. Sci.*, 2009, **3**, 104–108, DOI: **10.1007/s11706-009-0036-x**.
3 I. Ben Shir, S. Kababya, I. Katz, B. Pokroy and A. Schmidt, Exposed and Buried Biomineral Interfaces in the Aragonitic Shell of Perna canaliculus Revealed by Solid-State NMR, *Chem. Mater.*, 2013, **25**, 4595–4602, DOI: **10.1021/cm4028226**.
4 E. Beniash, J. Aizenberg, L. Addadi and S. Weiner, Amorphous calcium carbonate transforms into calcite during sea urchin larval spicule growth, *Proc. R. Soc. London, Ser. B*, 1997, **264**, 461–465, DOI: **10.1098/rspb.1997.0066**.
5 L. Addadi, S. Raz and S. Weiner, Taking Advantage of Disorder: Amorphous Calcium Carbonate and Its Roles in Biomineralization, *Adv. Mater.*, 2003, **15**, 959–970, DOI: **10.1002/adma.200300381**.
6 Y.-Q. Niu, J.-H. Liu, C. Aymonier, S. Fermani, D. Kralj, G. Falini and C.-H. Zhou, Calcium carbonate: controlled synthesis, surface functionalization, and nanostructured materials, *Chem. Soc. Rev.*, 2022, **51**, 7883–7943, DOI: **10.1039/D1CS00519G**.
7 A. Herman, L. Addadi and S. Weiner, Interactions of sea-urchin skeleton macromolecules with growing calcite crystals—a study of intracrystalline proteins, *Nature*, 1988, **331**, 546–548, DOI: **10.1038/331546a0**.
8 I. M. Weiss, N. Tuross, L. Addadi and S. Weiner, Mollusc larval shell formation: amorphous calcium carbonate is a precursor phase for aragonite, *J. Exp. Zool.*, 2002, **293**, 478–491, DOI: **10.1002/jez.90004**.

9 S. Raz, S. Weiner and L. Addadi, Formation of High-Magnesian Calcites *via* an Amorphous Precursor Phase: Possible Biological Implications, *Adv. Mater.*, 2000, **12**, 38–42, DOI: **10.1002/(SICI)1521-4095(200001)12:1<38::AID-ADMA38>3.0.CO;2-I**.

10 G. Falini, M. Gazzano and A. Ripamonti, Crystallization of calcium carbonate in presence of magnesium and polyelectrolytes, *J. Cryst. Growth*, 1994, **137**, 577–584, DOI: **10.1016/0022-0248(94)91001-4**.

11 E. Seknazi and B. Pokroy, Residual Strain and Stress in Biocrystals, *Adv. Mater.*, 2018, **30**, 1–6, DOI: **10.1002/adma.201707263**.

12 Y. Politi, D. R. Batchelor, P. Zaslansky, B. F. Chmelka, J. C. Weaver, I. Sagi, S. Weiner and L. Addadi, Role of Magnesium Ion in the Stabilization of Biogenic Amorphous Calcium Carbonate: A Structure–Function Investigation, *Chem. Mater.*, 2010, **22**, 161–166, DOI: **10.1021/cm902674h**.

13 J. Aizenberg, A. Tkachenko, S. Weiner, L. Addadi and G. Hendler, Calcitic microlenses as part of the photoreceptor system in brittlestars, *Nature*, 2001, **412**, 819–822, DOI: **10.1038/35090573**.

14 I. Polishchuk, A. A. Bracha, L. Bloch, D. Levy, S. Kozachkevich, Y. Etinger-Geller, Y. Kauffmann, M. Burghammer, C. Giacobbe, J. Villanova, G. Hendler, C. Y. Sun, A. J. Giuffre, M. A. Marcus, L. Kundanati, P. Zaslansky, N. M. Pugno, P. U. P. A. Gilbert, A. Katsman and B. Pokroy, Coherently aligned nanoparticles within a biogenic single crystal: A biological prestressing strategy, *Science*, 1979, **358**(2017), 1294–1298, DOI: **10.1126/science.aaj2156**.

15 E. Seknazi, S. Kozachkevich, I. Polishchuk, N. Bianco Stein, J. Villanova, J.-P. Suuronen, C. Dejoie, P. Zaslansky, A. Katsman and B. Pokroy, From spinodal decomposition to alternating layered structure within single crystals of biogenic magnesium calcite, *Nat. Commun.*, 2019, **10**, 4559, DOI: **10.1038/s41467-019-12168-8**.

16 N. Bianco-Stein, I. Polishchuk, A. Lang, L. Portal, C. Dejoie, A. Katsman and B. Pokroy, High-Mg calcite nanoparticles within a low-Mg calcite matrix: A widespread phenomenon in biomineralization, *Proc. Natl. Acad. Sci. U. S. A.*, 2022, **119**, 16, DOI: **10.1073/pnas.2120177119**.

17 J. C. Weaver, G. W. Milliron, A. Miserez, K. Evans-Lutterodt, S. Herrera, I. Gallana, W. J. Mershon, B. Swanson, P. Zavattieri, E. DiMasi and D. Kisailus, The stomatopod dactyl club: A formidable damage-tolerant biological hammer, *Science*, 1979, **336**(2012), 1275–1280, DOI: **10.1126/science.1218764**.

18 S. N. Patek and R. L. Caldwell, Extreme impact and cavitation forces of a biological hammer: Strike forces of the peacock mantis shrimp Odontodactylus scyllarus, *J. Exp. Biol.*, 2005, **208**, 3655–3664, DOI: **10.1242/jeb.01831**.

19 Z. Chen, Z. Li, J. Li, C. Liu, C. Lao, Y. Fu, C. Liu, Y. Li, P. Wang and Y. He, 3D printing of ceramics: A review, *J. Eur. Ceram. Soc.*, 2019, **39**, 661–687, DOI: **10.1016/j.jeurceramsoc.2018.11.013**.

20 C. Minas, D. Carnelli, E. Tervoort and A. R. Studart, 3D Printing of Emulsions and Foams into Hierarchical Porous Ceramics, *Adv. Mater.*, 2016, **28**, 9993–9999, DOI: **10.1002/adma.201603390**.

21 L. Alison, S. Menasce, F. Bouville, E. Tervoort, I. Mattich, A. Ofner and A. R. Studart, 3D printing of sacrificial templates into hierarchical porous materials, *Sci. Rep.*, 2019, **9**, 409, DOI: **10.1038/s41598-018-36789-z**.

22 A. R. Studart, Biological and bioinspired composites with spatially tunable heterogeneous architectures, *Adv. Funct. Mater.*, 2013, **23**, 4423–4436, DOI: **10.1002/adfm.201300340**.

23 J. Liu, O. Erol, A. Pantula, W. Liu, Z. Jiang, K. Kobayashi, D. Chatterjee, N. Hibino, L. H. Romer, S. H. Kang, T. D. Nguyen and D. H. Gracias, Dual-Gel 4D Printing of Bioinspired Tubes, *ACS Appl. Mater. Interfaces*, 2019, **11**, 8492–8498, DOI: **10.1021/acsami.8b17218**.

24 H. Guo, A. Baker, J. Guo and C. A. Randall, Cold Sintering Process: A Novel Technique for Low-Temperature Ceramic Processing of Ferroelectrics, *J. Am. Ceram. Soc.*, 2016, **99**, 3489–3507, DOI: **10.1111/jace.14554**.

25 Y. S. Han, J. B. Li, Q. M. Wei and K. Tang, The effect of sintering temperatures on alumina foam strength, *Ceram. Int.*, 2002, **28**, 755–759, DOI: **10.1016/S0272-8842(02)00039-1**.

26 I. B. Cutler, C. Bradshaw, C. J. Christensen and E. P. Hyatt, Sintering of Alumina at Temperatures of 1400 °C. and Below, *J. Am. Ceram. Soc.*, 1957, **40**, 134–139, DOI: **10.1111/j.1151-2916.1957.tb12589.x**.

27 C. Nething, M. Smirnova, J. A. D. Gröning, W. Haase, A. Stolz and W. Sobek, A method for 3D printing biocemented spatial structures using sand and urease active calcium carbonate powder, *Mater. Des.*, 2020, **195**, 109032, DOI: **10.1016/j.matdes.2020.109032**.

28 H. Yang, Y. Che and M. Shi, Influences of calcium carbonate nanoparticles on the workability and strength of 3D printing cementitious materials containing limestone powder, *J. Build. Eng.*, 2021, **44**, 102976, DOI: **10.1016/j.jobe.2021.102976**.

29 T. Wang, J. Zheng, T. Hu, H. Zhang, K. Fu, R. Yin and W. Zhang, Three-Dimensional Printing of Calcium Carbonate/Hydroxyapatite Scaffolds at Low Temperature for Bone Tissue Engineering, *3D Print. Addit. Manuf.*, 2021, **8**, 1–13, DOI: **10.1089/3dp.2020.0140**.

30 Z. Geng, W. She, W. Zuo, K. Lyu, H. Pan, Y. Zhang and C. Miao, Layer-interface properties in 3D printed concrete: Dual hierarchical structure and micromechanical characterization, *Cem. Concr. Res.*, 2020, **138**, 106220, DOI: **10.1016/j.cemconres.2020.106220**.

31 T. Marchment, J. Sanjayan and M. Xia, Method of enhancing interlayer bond strength in construction scale 3D printing with mortar by effective bond area amplification, *Mater. Des.*, 2019, **169**, 107684, DOI: **10.1016/j.matdes.2019.107684**.

32 V. N. Nerella and V. Mechtcherine, MICRO-AND MACROSCOPIC INVESTIGATIONS ON THE INTERFACE BETWEEN LAYERS OF 3D-PRINTED CEMENTITIOUS ELEMENTS-Project B1 View project Application of Carbon nano tubes in geopolymers View project, (2017). **https://www.researchgate.net/publication/319504633** (accessed January 2, 2023).

33 G. Li, A new way to increase the long-term bond strength of new-to-old concrete by the use of fly ash, *Cem. Concr. Res.*, 2003, **33**, 799–806, DOI: **10.1016/S0008-8846(02)01064-5**.
34 B.-W. Jo, C.-H. Kim, G. Tae and J.-B. Park, Characteristics of cement mortar with nano-SiO_2 particles, *Constr. Build. Mater.*, 2007, **21**, 1351–1355, DOI: **10.1016/j.conbuildmat.2005.12.020**.
35 D. R. Morgan, Compatibility of concrete repair materials and systems, *Constr. Build. Mater.*, 1996, **10**, 57–67, DOI: **10.1016/0950-0618(95)00060-7**.
36 H. Shaked, I. Polishchuk, A. Nagel, Y. Bekenstein and B. Pokroy, Long-term stabilized amorphous calcium carbonate—an ink for bio-inspired 3D printing, *Mater. Today Bio*, 2021, **11**, 100120, DOI: **10.1016/j.mtbio.2021.100120**.
37 ASTM International, C1161-13: Standard Test Method for Flexural Strength of Advanced Ceramics at Ambient, Annual Book of ASTM Standards 11 (2008) 1–16. 10.1520/C1161-13.
38 N. Bianco-Stein, I. Polishchuk, G. Seiden, J. Villanova, A. Rack, P. Zaslansky and B. Pokroy, Helical Microstructures of the Mineralized Coralline Red Algae Determine Their Mechanical Properties, *Adv. Sci.*, 2020, **7**, 2000108, DOI: **10.1002/advs.202000108**.
39 M. Albéric, L. Bertinetti, Z. Zou, P. Fratzl, W. Habraken and Y. Politi, The Crystallization of Amorphous Calcium Carbonate is Kinetically Governed by Ion Impurities and Water, *Adv. Sci.*, 2018, **5**, 5, DOI: **10.1002/advs.201701000**.
40 C.-J. Lin, S.-Y. Yang, S.-J. Huang and J. C. C. Chan, Structural Characterization of Mg-Stabilized Amorphous Calcium Carbonate by Mg-25 Solid-State NMR Spectroscopy, *J. Phys. Chem. C*, 2015, **119**, 7225–7233, DOI: **10.1021/jp512971a**.
41 L. Krounbi, K. Hedderick, Z. Eyal, L. Aram, E. Shimoni, L. A. Estroff and A. Gal, Surface-induced coacervation facilitates localized precipitation of mineral precursors from dilute solutions, *Chem. Mater.*, 2020, **33**, 10, DOI: **10.1021/acs.chemmater.0c04668**.
42 R. A. Turusov, V. I. Andreev and N. Yu Tsybin, A Composite of Layered Structure. Transversal Strength and Young's Modulus, *Polym. Sci., Ser. D*, 2022, **15**, 10–18, DOI: **10.1134/S1995421222010233**.
43 I. Galan, F. P. Glasser and C. Andrade, Calcium carbonate decomposition, *J. Therm. Anal. Calorim.*, 2013, **111**, 1197–1202, DOI: **10.1007/s10973-012-2290-x**.